Chinese Chemical Letters 37 (2026) 112034

Contents lists available at ScienceDirect

Chinese Chemical Letters

journal homepage: www.elsevier.com/locate/cclet

Portal-directed assembly of 2D cucurbituril-polyoxometalate hybrids toward synergistic photothermal catalysis

Fei Li, Yibin Sun*, Bao Li, Siyuan Xu, Shuangyu Wu, Lixin Wu*, Guanglu Wu*

State Key Laboratory of Supramolecular Structure and Materials, College of Chemistry, Jilin University, Changchun 130012, China

ARTICLE INFO

Article history:
Received 8 August 2025
Revised 20 October 2025
Accepted 29 October 2025
Available online 29 October 2025

Keywords:
Cucurbit[*n*]urils
Polyoxometalates
Hybrids
Dimensional control
Photothermal catalysis

ABSTRACT

Precise control over the dimensionality and morphology of supramolecular assemblies remains a key challenge in hybrid material design. Here we report a directional assembly strategy that exploits synergistic portal-specific hydrogen bonding and ion–dipole interactions between cucurbit[5]uril (CB[5]) and an Anderson-type polyoxometalate (POM) functionalized with terminal protonated amines. This tailored interaction drives the formation of elongated two-dimensional hybrid sheets with spatial confinement and anisotropic growth. The resulting CB[5]-NH_2POM hybrids exhibit high thermal stability and surface-accessible CB[5] units, enabling hierarchical integration with gold nanorods (AuNRs). These AuNRs@CB[5]-NH_2POM hybrids demonstrate efficient photothermal conversion (37.8 %) and enable near-quantitative catalytic conversion (>99 %) in NIR-triggered sulfide oxidation. Comparative controls confirm the critical role of CB[5]-mediated portal interactions in both structural definition and functional performance. This study highlights a transferable supramolecular design principle for dimensional control and modular interface engineering, offering a promising platform for developing adaptive hybrid materials in photothermal catalysis and related applications.

© 2026 Published by Elsevier B.V. on behalf of Chinese Chemical Society and Institute of Materia Medica, Chinese Academy of Medical Sciences.

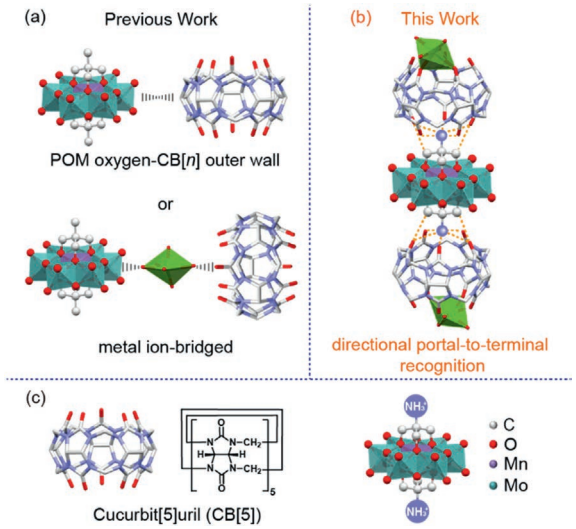
The rational design of hybrid materials, especially those combining organic and inorganic components, offers exciting opportunities in catalysis [1–5], optoelectronics [6–8], energy conversion [9–12] and information storage [13–15]. Such materials can integrate complementary functions, yet their practical utility often hinges on a persistent challenge: the ability to precisely engineer structural hierarchy at the molecular level [16–19]. In particular, achieving long-range structural order and well-defined dimensionality in supramolecular hybrids remains difficult to realize, especially in systems governed by multiple, competing noncovalent interactions [20–25].

One promising approach to structural control in supramolecular hybrids involves the use of macrocyclic hosts such as cyclodextrins [26,27], calixarenes [28], pillararenes [29], and cucurbit[*n*]urils (CB[*n*]s) [30,31], which offer well-defined geometries and interactive sites [32,33]. When combined with polyoxometalates (POMs) [34,35], redox-active [36,37] and thermally stable [38] metal-oxide clusters, these macrocycles enable the assembly of organic–inorganic hybrid materials *via* diverse noncovalent interactions, including ion–dipole attraction [39–41], hydrogen bonding [42–44], and host–guest recognition [45–47]. Among these, CB[*n*]-POM hybrids stand out for their rich interaction landscapes and modularity [39,46,48–51]. However, most reported assemblies are constructed through isotropic interaction modes such as nonspecific electrostatic pairing [41,52–56] or metal-ion bridging (Scheme 1a) [57–60]. These modes offer little spatial selectivity, making it difficult to guide assembly along a specific spatial direction or to control the resulting dimensionality. As a result, these hybrids typically exhibit compact, non-elongated structures that offer limited opportunities for hierarchical organization or interface engineering [61,62].

Herein, we report a molecular design that enables anisotropic assembly of CB[*n*]-POM hybrids through spatially defined dual noncovalent interactions, namely hydrogen bonding and ion–dipole interactions. By introducing primary amino groups at both termini of an Anderson-type POM, their protonated form (–NH_3^+) enables strong interactions with the carbonyl portals of CB[5] (Scheme 1b), thereby breaking the symmetry of interfacial interactions and promoting the formation of elongated two-dimensional (2D) architectures. This portal-specific interaction not only governs the growth direction at the molecular level but also preserves the accessibility of CB[5] units on the hybrid surface. As a result, the

* Corresponding authors.
E-mail addresses: yibinsun@jlu.edu.cn (Y. Sun), wulx@jlu.edu.cn (L. Wu), guanglu@jlu.edu.cn (G. Wu).

https://doi.org/10.1016/j.cclet.2025.112034
1001-8417/© 2026 Published by Elsevier B.V. on behalf of Chinese Chemical Society and Institute of Materia Medica, Chinese Academy of Medical Sciences.



Scheme 1. Interaction modes for CB[*n*]-POM assemblies. (a) Common interaction modes in previously reported CB[*n*]-POM assemblies, including ion–dipole contacts and hydrogen bonds between POM surface oxygens with the outer wall of CB[*n*], or metal ion-bridged linkages between POM and CB[*n*] portals. These modes are typically isotropic and lack spatial control. (b) This work: Directional portal-to-terminal hydrogen bonding and ion–dipole interactions between CB[5] carbonyl portals and the terminal protonated amino groups of a functionalized Anderson-type POM enables anisotropic assembly. (c) Molecular structures of the two building blocks used in this study.

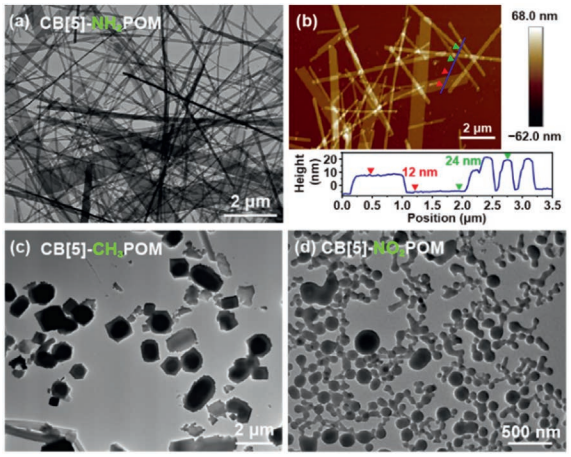


Fig. 1. Morphology of CB[5]-POM hybrid assemblies. (a) TEM image of CB[5]-NH_2POM reveals the formation of extended, sheet-like structures with high aspect ratios. (b) AFM image of CB[5]-NH_2POM confirming the sheet-like structures with a typical layer thickness of ~12 nm. (c, d) In contrast, TEM images of CB[5]-CH_3POM and CB[5]-NO_2POM hybrids exhibit irregular, non-elongated morphologies.

assembled 2D structures serve as versatile platforms for hierarchical integration with gold nanorods (AuNRs), enabling cooperative photothermal catalysis with enhanced stability and selectivity.

Achieving such controlled dimensional growth in supramolecular hybrids requires carefully engineered, spatially selective interactions at the molecular level [15,16,20,22]. In the case of CB[*n*]-POM systems, however, both the outer surface of CB[*n*] and the POM core carry symmetrically distributed charges and are generally inert to site-specific functionalization. This isotropic interaction landscape makes it challenging to direct assembly along a preferred spatial axis [39,46,48,49].

To address this issue, we selected Anderson-type polyoxometalates, which feature chemically accessible termini that can be selectively modified. We introduced primary amino groups at both ends of the Anderson cluster to afford $Na_3[MnMo_6O_{18}((OCH_2)_3CNH_2)_2]$, hereafter referred to as NH_2POM [63–65]. In aqueous solution, the amino groups are protonated (Scheme 1c) and engage in strong, directional hydrogen bonding as well as ion–dipole interactions with the carbonyl-lined portals of CB[5], thereby enhancing binding strength along a specific axis and introducing directional selectivity in the assembly kinetics.

Upon mixing equimolar aqueous solutions of CB[5] and NH_2POM, a white suspension formed immediately, indicating rapid self-assembly. Transmission electron microscopy (TEM) revealed the resulting hybrid, CB[5]-NH_2POM, as elongated, sheet-like structures with lateral dimensions ranging from 1 μm to 12 μm and widths of 70 nm to 1 μm (Fig. 1a). Atomic force microscopy (AFM) confirmed a layer thickness of ~12 nm (Fig. 1b), and SEM-EDS analysis verified the co-presence of both components in the material (Fig. S1 in Supporting information).

To validate the role of dual-interaction in guiding this anisotropic growth, we synthesized two control POM analogues: CH_3POM and NO_2POM, in which the amino groups were replaced with methyl and nitro substituents, respectively. These modifications disrupt the ability of POM's termini to form hydrogen bonds and ion–dipole interactions with CB[5] portals. As anticipated, TEM images of CB[5]-CH_3POM and CB[5]-NO_2POM showed relatively irregular, non-extended morphologies lacking the ordered, sheet-like features of CB[5]-NH_2POM (Figs. 1c and d).

We also examined the effect of CB[*n*] portal size and geometry. CB[5] features a compact portal lined with five carbonyl groups that support spatially confined interactions, whereas larger homologues such as CB[6] and CB[7] possess wider portals with more diffuse charge distribution and increased steric freedom. When NH_2POM was combined with CB[6] or CB[7], no 2D morphology formed; instead, TEM showed irregular, aggregated structures (Fig. S2 in Supporting information), highlighting CB[5] as uniquely suited for promoting anisotropic assembly *via* dual-interaction alignment.

To probe the molecular basis of this growth directionality, we obtained single crystals of CB[5]-NH_2POM. The resolved structure revealed a repeating unit comprising one protonated NH_2POM, two CB[5] molecules, and two Na^+ ions (Figs. 2a-d). Each NH_3^+ terminus forms five N–H···O hydrogen bonds (2.843–2.905 Å) with the carbonyl portal of CB[5], while simultaneously engaging in ion–dipole interactions with the same region. In addition, the methylene groups adjacent to the NH_3^+ of POM contribute further stabilization through C–H···O interactions (3.029–3.201 Å) (Fig. 2c, Figs. S3 and S4 in Supporting information). These interaction scaffolds act cooperatively as a spatially defined binding motif, imparting directionality to the assembly and driving its anisotropic elongation.

In addition to portal recognition, we identified a secondary interaction mode involving the CB[5] outer surface and oxygen-rich regions of NH_2POM (Fig. 2d and Fig. S5 in Supporting information). These include Mo=O···H–O hydrogen bonds (2.951 Å) with water coordinated to Na^+, Mo–O/Mo=O···H–C contacts (2.981–3.173 Å) with CB[5] methylene groups, and ion–dipole interactions (Mo=O···N, 2.954 Å) with nitrogen atoms embedded in the CB[5] scaffold. These weaker, cooperative forces contribute to lateral association, reinforcing the 2D framework.

To clarify the role of portal binding, we tried to prepare single crystals for the two control hybrids, CB[5]-CH_3POM and CB[5]-NO_2POM. In CB[5]-CH_3POM, where the terminal NH_2 groups are replaced by non-binding methyl groups, single-crystal analysis confirmed that interactions occur exclusively at the CB[5] outer surface, with no portal engagement (Figs. 2e–g). The Mo–O/Mo=O···H–C contacts observed (2.965–3.200 Å) were uniformly distributed and failed to induce directional growth, resulting in non-elongated structures (Fig. 2g). Besides non-extended mor-

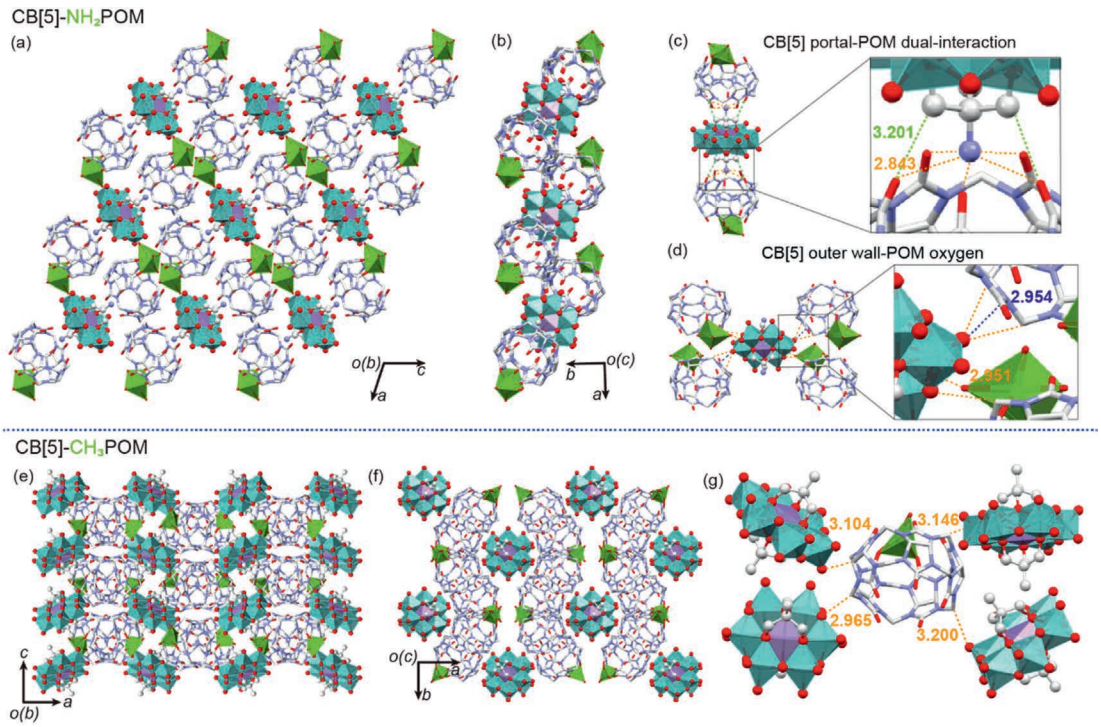


Fig. 2. Molecular-level analysis of CB[5]-POM hybrids. (a, b) Single-crystal structure of CB[5]-NH_2POM, showing a highly ordered framework composed of alternating CB[5] and POM units. (c) Enlarged view of the portal-to-terminal hydrogen bonding between CB[5] carbonyl portals and the protonated amino (orange, 2.843 Å) and methylene (green, 3.201 Å) groups of NH_2POM. (d) Additional noncovalent interactions between the outer surface of CB[5] and oxygen atoms on NH_2POM. Blue: ion–dipole interactions, orange: hydrogen bonds. (e, f) Single-crystal structure of CB[5]-CH_3POM, which lacks portal binding and exhibits a more isotropic packing pattern. (g) Detailed view of Mo–O/Mo=O···H–C hydrogen bonds between POM oxygen atoms and the outer wall of CB[5]. All hydrogen atoms and crystallographically irrelevant water molecules are omitted for clarity. Bond distances are shown in Å.

phology observed in TEM (Fig. 1d), CB[5]-NO_2POM did not yield crystals at all, which we attribute to the electron-withdrawing effect of nitro groups, leading to reduced local electrostatic potential and weakened noncovalent interactions with CB[5] [66,67].

Taken together, these observations reveal two dominant interaction directions: One driven by portal-localized hydrogen bonding and ion–dipole interactions, the other by weaker peripheral interactions. We propose that these define the principal growth axes of the 2D sheets, with the average portal-to-terminal direction exhibiting the fastest propagation, consistent with the elongated morphology. This hypothesis is supported by PXRD measurements, which show a sharp reflection at $2\theta = 5.6°$, matching the (020) plane predicted from the crystal structure (Fig. S6 in Supporting information). The angle between this plane and the portal-to-terminal directions is $\pm 33.3°$, indicating that it corresponds to the averaged growth direction governed by portal-to-terminal dual-interaction (Fig. S7 in Supporting information), affirming its role as the primary driver of anisotropic assembly in the CB[5]-NH_2POM system.

Because the CB[5] portals are oriented at an angle relative to the preferred growth direction and only one portal is occupied by NH_2POM (while the other is only partially coordinated with Na^+ ion), multiple CB[5] units remain exposed on the CB[5]-NH_2POM nanosheet surface. These exposed units provide accessible and spatially arranged binding sites for further functional integration. Given previous reports on CB[*n*] interactions with gold nanorods (AuNRs), the array of CB[5] outer surface as well as their partially exposed portals are expected to facilitate efficient AuNRs anchoring [68–70]. Moreover, the negatively charged centers of NH_2POM can interact electrostatically with the CTAB-coated AuNRs, further promoting their loading. To investigate this, we examined the hierarchical assembly of CTAB-stabilized AuNRs (average length ≈ 65 nm, Fig. S8 in Supporting information) onto the hybrid sheets (Fig. 3a).

Upon mixing with CB[5]-NH_2POM suspensions, TEM imaging showed AuNRs decorated on the sheet surface, with little deposition observed on the carbon support film (Fig. 3b), indicating the specific loading. UV–vis spectroscopy further confirmed the integration, showing a redshift and broadening of the longitudinal plasmon resonance band (from 740 nm to 785 nm) due to plasmonic coupling among closely spaced nanorods on the nanosheet surface (Fig. S9 in Supporting information) [71–72].

Notably, the assembled hybrid displayed outstanding thermal robustness. After heating the AuNRs@CB[5]-NH_2POM composites at 60 °C for 3 h, both the nanosheet morphology and AuNRs distribution remained intact (Fig. 3c). This contrasts with control hybrids: CB[5]-CH_3POM, where interaction occurs only on the outer surface of CB[5], and CB[5]-NO_2POM, where strong electron-withdrawing substituents weaken interfacial binding. Neither control exhibited the ability to maintain ordered structure or morphological integrity under identical thermal treatment (Fig. S10 in Supporting information). PXRD analysis provided consistent evidence: The CB[5]-NH_2POM assembly maintained its crystallinity after treatment, CB[5]-CH_3POM exhibited a pronounced loss of crystallinity upon heating, while CB[5]-NO_2POM showed no crystalline signals at all (Fig. S11 in Supporting information). These results underscore the key role of portal-localized dual-interaction in conferring stability and structural coherence.

Having established a robust and thermally stable hybrid platform with spatially integrated AuNRs, we next evaluated its performance in photothermal catalysis. The two components: POMs and AuNRs, offer complementary functionalities: POMs serve as redox-active catalysts for selective oxidation, while AuNRs efficiently convert near-infrared (NIR) light into localized heat *via* plasmonic resonance [73–75]. Their co-localization within a 2D framework enables synergistic behavior not achievable by either component alone.

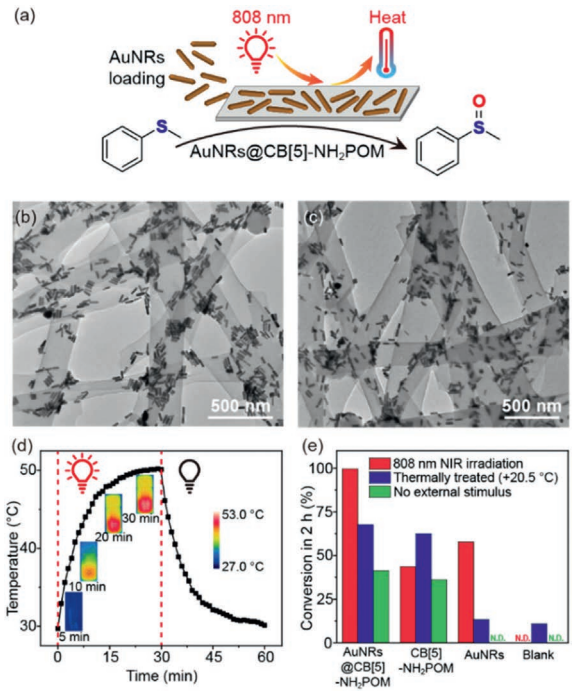


Fig. 3. Photothermal performance and catalytic behavior of AuNRs@CB[5]-NH_2POM hybrids. (a) Schematic illustration of AuNRs loading onto CB[5]-NH_2POM nanosheets and their application in near-infrared (808 nm) light-triggered sulfide oxidation. (b) TEM image of AuNRs@CB[5]-NH_2POM, showing the specific distribution of AuNRs across the 2D nanosheet surface. (c) TEM image after heating at 60 °C for 3 h, confirming preservation of both nanosheet morphology and nanoparticle attachment. (d) Photothermal heating profile of AuNRs@CB[5]-NH_2POM under near-infrared laser irradiation (808 nm, 1.0 W/cm^2), with thermal images at selected time points inset. (e) Conversion rates of benzyl sulfide to sulfoxide under three conditions—NIR irradiation, thermal treatment (+20.5 °C), and no external stimulus—comparing the catalytic performance of AuNRs@CB[5]-NH_2POM, CB[5]-NH_2POM, AuNRs alone, and a blank control.

Under NIR irradiation at 808 nm (1.0 W/cm^2), a suspension of AuNRs@CB[5]-NH_2POM (CB[5], 200 μmol/L, 1 mL; Au, 0.223 equiv.) exhibited a rapid temperature increase of 20.5 °C within 30 min, while control samples (pure water or CB[5]-NH_2POM alone) showed only minor heating (~3.4 °C) (Fig. 3d, Figs. S12 and S13 in Supporting information). This corresponds to a photothermal conversion efficiency of 37.8 % in AuNRs@CB[5]-NH_2POM hybrids, calculated from the heating–cooling profile (see Supporting information for details). The high efficiency arises from plasmonic coupling among incorporated AuNRs and the thermal stability of the CB[5]-based interface, which ensures structural integrity and supports effective energy transfer.

We then applied this hybrid to the selective oxidation of thioanisole into methyl phenyl sulfoxide, a model reaction relevant to organic synthesis [76–79] and biomedicine (Fig. 3a) [80–82]. A mixture of AuNRs@CB[5]-NH_2POM and thioanisole (CB[5], 200 μmol/L, 1 mL; Au, 0.014 equiv.; thioanisole, 310 equiv.) in water was irradiated for 2 h with an 808 nm laser. After extraction and analysis, ^{1}H NMR revealed a conversion rate of greater than 99 % (Fig. 3e and Fig. S14 in Supporting information), significantly outperforming all controls: CB[5]-NH_2POM (43.6 %), AuNRs alone (57.8 %), and blank (N.D.). Notably, control samples without AuNRs still showed a modest increase in conversion under 808 nm laser, attributable to the slight temperature rise (~3.4 °C) induced by NIR irradiation. As a thermal control, all catalyst systems were subjected to heating from 29.7 °C with a temperature increase of 20.5 °C, matching that observed in the photothermal conversion experiment of AuNRs@CB[5]-NH_2POM (Au, 8.8 ppm, 1.0 mL), with overheating ensuring the comparability of conditions. For AuNRs-containing samples, however, the catalytic efficiency under thermal treatment remained lower than that under NIR irradiation, even with overheating, confirming the superior effect of localized photothermal heating [73]. These results establish AuNRs@CB[5]-NH_2POM as an efficient, selective, and thermally stable photothermal catalyst, capable of harnessing both component functionalities through spatial integration and structural coherence.

In summary, we have demonstrated a rational molecular design strategy for constructing well-defined 2D supramolecular hybrids through portal-to-terminal hydrogen bonding and ion–dipole interactions between CB[5] and a terminally aminated Anderson-type POM. This spatially directed interaction not only governs the anisotropic growth of CB[5]-NH_2POM into elongated 2D sheets, but also preserves the accessibility of CB[5] sites on the hybrid surface, enabling hierarchical integration with gold nanorods. The resulting hybrid exhibits outstanding thermal stability, specific nanoparticle anchoring, and efficient photothermal conversion (37.8 %), which together translate into highly selective catalytic performance (>99 % conversion) in NIR-triggered sulfide oxidation. Comparative analysis with non-dual-interaction POM analogues and larger CB[*n*]s highlights the unique role of CB[5]-mediated portal-to-terminal interactions in achieving both structural order and functional enhancement.

This work highlights the structural and functional advantages of introducing noncovalent directionality into macrocycle–cluster assemblies, and suggests a transferable design strategy for systems where dimensional control and interface modularity are critical. The underlying principles demonstrated here could support future efforts in the development of adaptive hybrid materials for applications in photothermal catalysis, smart nanoreactors, and integrated energy conversion systems.

Declaration of competing interest

The authors declare no competing financial interest.

CRediT authorship contribution statement

Fei Li: Writing – review & editing, Writing – original draft, Investigation, Data curation, Conceptualization. **Yibin Sun:** Writing – review & editing, Writing – original draft, Conceptualization. **Bao Li:** Data curation. **Siyuan Xu:** Investigation, Data curation. **Shuangyu Wu:** Investigation. **Lixin Wu:** Writing – review & editing, Writing – original draft, Methodology, Funding acquisition, Conceptualization. **Guanglu Wu:** Writing – review & editing, Writing – original draft, Methodology, Funding acquisition, Conceptualization.

Acknowledgments

This work was supported by the National Key R&D Program of China (No. 2021YFA1501600, G. Wu), the National Natural Science Foundation of China (No. 22171103 for G. Wu, No. 22271117 for L. Wu, and No. 22301010 for Y.S.), and the Natural Science Foundation of Jilin Province (No. 202301002, G. Wu). The authors gratefully acknowledge the Shanghai Synchrotron Radiation Facility (beamline BL17B, proposal 2023-NFPS-PT-500640) for experimental support.

Supplementary materials

Supplementary material associated with this article can be found, in the online version, at doi:10.1016/j.cclet.2025.112034.

References

[1] M. Yamaguchi, K. Shioya, C. Li, et al., J. Am. Chem. Soc. 146 (2024) 4549–4556.

[2] F. Hoffmann, M. Cornelius, J. Morell, M. Fröba, Angew. Chem. Int. Ed. 45 (2006) 3216–3251.
[3] Y.F. Liu, C.W. Hu, G.P. Yang, Chin. Chem. Lett. 34 (2023) 108097.
[4] C. Lian, S.H. Zhao, H.L. Li, X. Cao, Chin. Chem. Lett. 35 (2024) 109343.
[5] P. Wu, Y. Wang, B. Huang, Z. Xiao, Nanoscale 13 (2021) 7119–7133.
[6] X.J. Wang, B. Yin, L.R. Jiang, et al., Science 381 (2023) 784–790.
[7] D.M. Cheng, B. Li, S. Sun, et al., CCS Chem. 3 (2020) 1649–1658.
[8] K. Zhou, B.Y. Qi, Z.W. Liu, et al., Adv. Funct. Mater. 34 (2024) 2411671.
[9] B. Li, X.Z. Duan, D.M. Cheng, et al., J. Am. Chem. Soc. 145 (2023) 2243–2251.
[10] J.S. Huang, Y.B. Yuan, Y.C. Shao, Y.F. Yan, Nat. Rev. Mater. 2 (2017) 17042.
[11] D. Pakulski, A. Gorczyński, D. Brykczyńska, et al., Angew. Chem. Int. Ed. 62 (2023) e202305239.
[12] L. Liu, J. Huang, M. Zhang, et al., Small 21 (2025) 2504372.
[13] H. Lian, X.Z. Cheng, H.T. Hao, et al., Chem. Soc. Rev. 51 (2022) 1926–1982.
[14] J. Chen, S. Yao, B. Wang, et al., Angew. Chem. Int. Ed. 64 (2025) e202416759.
[15] J.V. Barth, G. Costantini, K. Kern, Nature 437 (2005) 671–679.
[16] Q.D. Liu, X. Wang, Angew. Chem. Int. Ed. 62 (2023) e202217764.
[17] M. Dreher, P.M. Dombrowski, M.W. Tripp, et al., Nat. Commun. 14 (2023) 1554.
[18] T. Govindaraju, M.B. Avinash, Nanoscale 4 (2012) 6102–6117.
[19] J. Luo, X. Sun, J.F. Yin, P. Yin, T. Liu, Giant 2 (2020) 100013.
[20] I. Insua, J. Bergueiro, A. Méndez-Ardoy, I. Lostalé-Seijo, J. Montenegro, Chem. Sci. 13 (2022) 3057–3068.
[21] D.P. August, R.A.W. Dryfe, S.J. Haigh, et al., Nature 588 (2020) 429–435.
[22] R. Chakrabarty, P.S. Mukherjee, P.J. Stang, Chem. Rev. 111 (2011) 6810–6918.
[23] F.H. Zhang, H.Y. Li, Z. Li, Q.D. Liu, X. Wang, Nat. Synth. 3 (2024) 1039–1048.
[24] Z. He, J. Su, Y.T. Wang, et al., J. Am. Chem. Soc. 146 (2024) 19998–20008.
[25] X.C. Li, H.M. Zhang, L.F. Chi, Adv. Mater. 31 (2019) 1804087.
[26] Z.X. Liu, Y. Liu, Chem. Soc. Rev. 51 (2022) 4786–4827.
[27] Y. Wu, E. Liu, C. Shi, J.F. Stoddart, CCS Chem. 7 (2025) 1935–1971.
[28] R. Kumar, A. Sharma, H. Singh, et al., Chem. Rev. 119 (2019) 9657–9721.
[29] T. Ogoshi, T. Yamagishi, Y. Nakamoto, Chem. Rev. 116 (2016) 7937–8002.
[30] H.G. Nie, Z. Wei, X.L. Ni, Y. Liu, Chem. Rev. 122 (2022) 9032–9077.
[31] Y. Sun, H. Fang, X. Lin, et al., CCS Chem. 4 (2021) 557–565.
[32] Z.C. Liu, S.K.M. Nalluri, J.F. Stoddart, Chem. Soc. Rev. 46 (2017) 2459–2478.
[33] J. Murray, K. Kim, T. Ogoshi, W. Yao, B.C. Gibb, Chem. Soc. Rev. 46 (2017) 2479–2496.
[34] M.T. Pope, A. Müller, Angew. Chem. Int. Ed. 30 (1991) 34–48.
[35] N.I. Gumerova, A. Rompel, Nat. Rev. Chem. 2 (2018) 0112.
[36] L.P. Cui, S. Zhang, Y. Zhao, et al., Nat. Commun. 16 (2025) 3674.
[37] M. Remmers, B. Mashtakov, S. Repp, et al., Angew. Chem. Int. Ed. 64 (2025) e202418864.
[38] Y.Y. Wang, Z.H. Yu, J. Xiong, K. Yan, X.B. Lu, Adv. Funct. Mater. 34 (2024) 2405880.
[39] Y. Huang, R.H. Gao, M. Liu, et al., Angew. Chem. Int. Ed. 60 (2021) 15166–15191.
[40] K. Grzhegorzhevskii, M. Haouas, M. Lion, et al., Chem. Commun. 59 (2023) 86–89.
[41] X.K. Fang, P. Kögerler, L. Isaacs, S. Uchida, N. Mizuno, J. Am. Chem. Soc. 131 (2009) 432–433.
[42] S. Khlifi, J. Marrot, M. Haouas, et al., J. Am. Chem. Soc. 144 (2022) 4469–4477.
[43] Y.L. Wu, R.F. Shi, Y.L. Wu, et al., J. Am. Chem. Soc. 137 (2015) 4111–4118.
[44] G. Yang, Y.C. Wu, Z.X. Lv, et al., Chem. Commun. 59 (2023) 788–791.
[45] C. Falaise, M.A. Moussawi, S. Floquet, et al., J. Am. Chem. Soc. 140 (2018) 11198–11201.
[46] W.M. Guan, G.X. Wang, B. Li, L.X. Wu, Coord. Chem. Rev. 481 (2023) 215039.
[47] Y. Ishii, Y. Takenaka, K. Konishi, Angew. Chem. Int. Ed. 43 (2004) 2702–2705.
[48] Y.M. Nie, L. Cao, W. Xia, et al., Inorg. Chem. Commun. 130 (2021) 108706.
[49] J. Lü, J.X. Lin, M.N. Cao, R. Cao, Coord. Chem. Rev. 257 (2013) 1334–1356.
[50] Y. Fan, J. Tan, C. Zou, et al., Chin. Chem. Lett. 36 (2025) 110101.
[51] X.L. Ni, X. Xiao, H. Cong, et al., Acc. Chem. Res. 47 (2014) 1386–1395.
[52] W.J. Wang, X.Q. Wang, J. Cao, et al., Chem. Commun. 54 (2018) 2098–2101.
[53] B.X. Han, C.Z. Wang, K. Chen, et al., CrystEngComm 16 (2014) 1615–1619.
[54] B.X. Han, C.Z. Wang, Y. Zhao, et al., Eur. J. Inorg. Chem. 2014 (2014) 831–835.
[55] X. Xia, W.W. Ge, H.Y. Chen, et al., New J. Chem. 43 (2019) 10297–10304.
[56] W. Xia, Y.M. Nie, N. Lei, et al., Inorg. Chim. Acta 523 (2021) 120418.
[57] J. Lü, J.X. Lin, X.L. Zhao, R. Cao, Chem. Commun. 48 (2012) 669–671.
[58] L.W. Han, J.X. Lin, Q. Yin, et al., Cryst. Growth Des. 16 (2016) 1213–1217.
[59] H.L. Cao, F.Y. Cai, H.B. Huang, B. Karadeniz, J. Lü, Inorg. Chem. Commun. 84 (2017) 164–167.
[60] M.J. Wei, H.Y. Zang, E.L. Zhou, et al., Dalton Trans. 45 (2016) 4989–4992.
[61] M.L. Xu, X.Y. Ao, C.C. Song, et al., Inorg. Chem. Front. 11 (2024) 1117–1122.
[62] S. Li, W. Xia, Y.Q. Zhang, Z. Tao, New J. Chem. 44 (2020) 11895–11900.
[63] P.R. Marcoux, B. Hasenknopf, J. Vaissermann, P. Gouzerh, Eur. J. Inorg. Chem. 2003 (2003) 2406–2412.
[64] J.W. Zhang, Y.C. Huang, G. Li, Y.G. Wei, Coord. Chem. Rev. 378 (2019) 395–414.
[65] M. Cao, J. Lin, J. Lü, et al., J. Hazard. Mater. 186 (2011) 948–951.
[66] S. Irle, T.M. Krygowski, J.E. Niu, W.H.E. Schwarz, J. Org. Chem. 60 (1995) 6744–6755.
[67] O. Exner, T.M. Krygowski, Chem. Soc. Rev. 25 (1996) 71–75.
[68] Q. An, G.T. Li, C.A. Tao, et al., Chem. Commun. (2008) 1989–1991.
[69] T.C. Lee, O.A. Scherman, Chem. Eur. J. 18 (2012) 1628–1633.
[70] S.T. Jones, R.W. Taylor, R. Esteban, et al., Small 10 (2014) 4298–4303.
[71] A.N. Shipway, M. Lahav, R. Gabai, I. Willner, Langmuir 16 (2000) 8789–8795.
[72] S.K. Ghosh, T. Pal, Chem. Rev. 107 (2007) 4797–4862.
[73] G.X. Wang, X.F. Chen, B. Li, L.X. Wu, Inorg. Chem. Front. 10 (2023) 1852–1862.
[74] K. Xia, T. Yatabe, K. Yonesato, et al., Angew. Chem. Int. Ed. 61 (2022) e202205873.
[75] H.L. Jia, A.X. Du, H. Zhang, et al., J. Am. Chem. Soc. 141 (2019) 5083–5086.
[76] M.C. Carreno, Chem. Rev. 95 (1995) 1717–1760.
[77] K. Kaczorowska, Z. Kolarska, K. Mitka, P. Kowalski, Tetrahedron 61 (2005) 8315–8327.
[78] E. Skolia, P.L. Gkizis, C.G. Kokotos, ChemPlusChem 87 (2022) e202200008.
[79] S. Yan, L. Qiao, L. Chen, W.J. Guo, H.Q. Peng, Smart Mol. (2025) e20250003.
[80] S. Caron, R.W. Dugger, S.G. Ruggeri, J.A. Ragan, D.H.B. Ripin, Chem. Rev. 106 (2006) 2943–2989.
[81] C. Jacob, Nat. Prod. Rep. 23 (2006) 851–863.
[82] Y.M. Li, S.A.E.A. Rizvi, D.Q. Hu, et al., Angew. Chem. Int. Ed. 58 (2019) 13499–13506.